Structure-from-Motion on shallow reefs and beaches: potential and limitations of consumer-grade drones to reconstruct topography and bathymetry

C. Gabriel David[1,*], Nina Kohl[1,2], Elisa Casella[3], Alessio Rovere[4], Pablo Ballesteros[1], and Torsten Schlurmann[1]

[1]Ludwig-Franzius-Institute of the Leibniz Universität Hannover, Hannover, Germany
[2]Blue C GmbH, Hannover, Germany
[3]ZMT, Leibniz Center for Tropical Marine Research, Bremen, Germany
[4]MARUM, Center for Marine Environmental Sciences, University of Bremen, Bremen, Germany
[*]david@lufi.uni-hannover.de

ABSTRACT

Reconstructing the topography of shallow underwater environments using Structure-from-Motion – Multi View Stereo (SfM-MVS) techniques applied to aerial imagery from Unmanned Aerial Vehicles (UAVs) is a challenging problem, as it involves non-linear distortions caused by water refraction. This study presents an experiment with aerial photographs collected with a consumer-grade UAV on the shallow-water reef of Fuvahmulah, the Maldives. Under conditions of rising tide, we surveyed the same portion of the reef in ten successive flights. For each flight, we used SfM-MVS to reconstruct the Digital Elevation Model (DEM) of the reef, and used the flight at low tide (where the reef is almost entirely dry) to compare the performance of DEM reconstruction under higher water levels. Our results show that differences with the reference DEM increase with increasing depth, but are substantially larger if no underwater ground control points are taken into account in the processing. Correcting our imagery with algorithms that account for refraction did not improve the overall accuracy of reconstruction. We conclude that reconstructing shallow-water reefs (less than $1\,\mathrm{m}$ depth) with consumer-grade SfM-MVSs and SfM-MVS is possible, but its precision is limited and strongly correlated with water depth. The best results are achieved when ground control points were placed both above and underwater and no refraction correction is used in our processing.

Introduction

Coral reefs are complex and highly biodiverse ecosystems. Reefs provide several significant ecosystem services, that amount to nearly 200,000 US dollars per acre per year (Costanza et al., 2014), that are put at risk by increasing stresses from both local and global factors (Fine et al., 2019). Natural hazards and anthropogenic pressures affect small islands' coastlines and the underwater marine environment surrounding them (Kench and Brander, 2006; Duvat and Magnan, 2019; David and Schlurmann, 2020). In the face of climate change, the increase in ocean temperatures is forecasted to lead to more extensive coral bleaching (Skirving et al., 2019), causing increased coral mortality (Hédouin et al., 2020). As coral reefs play an important role in the protection of low-lying islands from waves and wave energy (Ferrario et al., 2014), it is important to develop and assess the effectiveness and precision of new and low-cost techniques to monitor the evolution of reef areas over time. To this end, remote sensing from satellites or laser scanners and echosounders are often employed to analyze the status and temporal evolution of beaches and marine environments (Klemas, 2011; Colbo et al., 2014; Hedley et al., 2018; Panagou et al., 2020).

Single Beam Echosounder (SBES) or Multibeam Echosounder (MBES) sonar determine water depth by transmitting sound pulses into water. Survey grade MBES cover areas with a sensor covering a lateral area of $120-150^{\circ}$ to record bathymetry with a vertical resolution of $<1\%$ of the water depth (Colbo et al., 2014). However, survey grade echo sounder depend on vessel draft and are usually not suitable for shallow waters ($<4\,\mathrm{m}-5\,\mathrm{m}$ depth, Leon et al., 2015; David and Schlurmann, 2020). Consumer-grade SBES – for example used by fishers – have a smaller immersion depth but recorded water depths vary between centimeter to lower decimeter scale compared to ground-truth water depths (Bandini et al., 2018). Furthermore, SBES perform punctual measurements and thus do neither provide an areal overview of the surveyed marine area, nor color information for mapping of the site, which is particularly relevant in coral reefs.

Other bathymetric survey methods are operated from the beach: Terrestrial Laser Scanning (TLS) can record topography and bathymetry from a single device. The error of underwater measurements increases with distance to the device. Here, the measuring error is equal to the measured water depth for distances $\gtrsim 15\,\mathrm{m}$ (Panagou et al., 2020).

In recent years, drones have been applied more frequently to survey beaches or other coastal environments. For example, recent studies employing UAV-borne Light Detection and Ranging (LiDAR) achieved centimeter accuracy for riverine waters of less than 2 m depth (Mandlburger et al., 2020). Bathymetric reconstruction is independent of surface texture when using UAV-borne LiDAR measurements, leading to a more robust outcome compared to photogrammetric methods (Mandlburger, 2019). However, LiDAR-based data struggles with *"too shallow"* waters or increased hydrodynamic activity, such as whitecaps of broken waves (Klemas, 2011; Leon et al., 2015).

A major issue with UAV-borne LiDAR is that drone platforms carrying the devices are usually larger and have a high take-off weight, which often requires a higher-level drone operations permits. A more common way to employ UAV-borne data is therefore to use consumer-grade drones, collecting aerial photographs and processing them with the SfM-MVS reconstruction approach afterwards. SfM-MVS merges photogrammetric principles with advances in 3D computer vision algorithms (Carrivick et al., 2016). The SfM-MVS methods use aerial imagery to create precise and accurate three dimensional DEM of coastal areas (Murfitt et al., 2017; Casella et al., 2020; Talavera et al., 2020). However, reconstructing coastal areas with SfM-MVS techniques is mostly limited to dry beach areas. The biggest challenge of underwater photogrammetry is that light refracts on the water surface (Casella et al., 2016; Dietrich, 2017; Mandlburger, 2019). Refraction of light on the water surface is explained by Snell's Law, which several approaches have used to correct underwater DEMs to improve the reconstruction precision (Westaway et al., 2000; Woodget et al., 2015; Dietrich, 2017). In general, through-water photogrammetry in clear conditions is dependent on the Secchi depth (visibility by means of turbitidy) and on surface textures of underwater areas (Mandlburger, 2019). Bathymetric reconstruction in calmer and deeper waters is possible, but is characterized by large uncertainties and becomes more challenging with increasing water depth and hydrodynamic activity (Casella et al., 2016).

This study stems from a project dealing with sea level rise and associated impacts on small islands (Ratter et al., 2019; David and Schlurmann, 2020). The project focusses on obtaining field measurements with aerial surveys to evaluate sediment transport as natural sea level rise adaptation on the Maldivian reef island of Fuvahmulah. While

on-land (dry beach) areas were the main objective of the project, this work analyzes data collected on reef flats on Fuvamulah. Error metrics for varying water depths on reef flats are currently not available (David and Schlurmann, 2020). The purpose of this study is therefore to assess the quality of reconstructed underwater topographies (bathymetries) from a SfM-MVS algorithm for different water levels to be able to utilize this information in future studies. We used a consumer-grade drone to record the intertidal inner reef. We surveyed the same area in 10 flights, with varying water depth conditions. Contextually, we employed pressure sensors to constantly measure water depths and a Real-Time Kinematic (RTK) Global Navigation Satellite System (GNSS) system to measure the position of Ground Control Points (GCPs) throughout the entire study site with centimetre precision. The GCPs are later used to georeference the three dimensional model, obtained through the SfM-MVS and Multi-View Stereo (MVS) approach. We start surveying the dry reef at low tide and continue our surveys as water levels increase with the rising tide. In the analysis, the digital reconstruction of the dry reef serves as *"accurate"* reference topography. Comparing all following DEMs of the study site with increasing water depths with the dry reference DEM, we estimate errors of the SfM-MVS algorithm in the bathymetric reconstruction originating from increasing water depth. We test error estimates related to two different aligning techniques in the photogrammetric process, and evaluate the bathymetry reconstructions calculated with and without the use of published refraction correction algorithms.

Overall, this study aims at (a) assessing the potential and limitation of SfM-MVS algorithms to reconstruct underwater areas; (b) evaluating the benefits of refraction correction in near-shore coastal areas; and (c) increasing confidence in exploiting aerial imagery of clear, shallow waters for bathymetric reconstruction in photogrammetric procedures under field conditions.

Study area, material and methods

Survey-site and area of interest

This study was carried out on the reef island Fuvahmulah, one of the most southern islands of the Maldives (Indian Ocean). The island is located about 30 km south of the equator (latitude: −0.30°, longitude: 73.43°, see Fig. 1a). The Maldivian capital Malé is situated approximately 500 km north of the island, while the distance to the the southern tip of the Indian peninsula is about 1025 km (see Fig. 1b). Unlike most other inhabited islands of the Maldives, Fuvahmulah is not part of an atoll – it only consists of one main island and its fringing reef.

This study distinguishes between the survey site and the area of interest: The survey site is the entire area recorded by the UAV. The area of interest, on the other hand, focuses on the georeferenced area within the survey site and is influenced by the tide (see Fig. 2).

The survey site is on a shallow, inter-tidal reef on the west coast of Fuvahmulah. The water around Fuvahmulah is clear and provides aerial visibility of the submerged reef bottom – even in depths over 1 m. The study contains 10 flights, recorded on March 26th, 2019 between low-tide at around 11:00 and high tide at around 17:30. The tidal range of spring tide in March 2019 was 1.21 m (all tide data from UHSLC; Caldwell et al., 2015). The tidal range on the survey day was 0.76 m, allowing the reef to fall dry at low tide. The water level on the reef Δh is the difference between the first flight and the water level of each subsequent flight, derived from the sea level data (Table 1 summarizes the different water levels and water depths on the study site for each flight). On the survey day, the sky was constantly clear and sunset was at 18:10 (Holmgren et al., 2018, pvlib v0.7.2). Thus, lighting on site only depends on the solar azimuth and zenith (Fig. 1d). For the survey day, the fifth generation atmospheric reanalysis of the global climate (ERA5) of the Collaboration for Australian Weather and Climate Research (CAWCR) gives a significant off-shore wave height of 0.87 m to 1.00 m at 0° latitude and 73° longitude (C3S, 2017), which is at a distance of $\sim$ 60 km from Fuvahmulah.

The aerial surveys cover a distance of about 140 m to 150 m longshore and 70 m to 80 m cross-shore. Four cross-shore zones characterize the survey area: the upper beach zone is a vegetated beach ridge, fringing the entire island. It hosts palm trees and shrubs (see Fig. 2). A sandy beach of $\sim$ 10 m width follows seaside of the vegetated area. The downward sloping coral stone delimits the sandy beach from the fringing coral reef. The coral stone experiences wave run-up and can be considered a natural revetment between mean sea levels and mean high waters for the nearby beaches. The inter-tidal reef has three longshore sections: On the right side, inhabitants of the island have cut a channel into the reef. The channel provided safe landing for boats before the seaport opened in 2002 (Ratter et al., 2019; David and Schlurmann, 2020). This area is constantly submerged and has the highest water depth of the study site. The channel bottom is sandy near the beach but becomes increasingly more rocky seaward. The excavated rocks from the channel construction were dumped adjacent to the channel along the entire reef and remained there until today. In this longshore area, only the 15 m long inner reef flat section close to the beach is clear

Table 1. Overview of water levels and average water depth on the reef within the study site (hydrostatic conditions). Sea level z_{SL} measurements at pressure sensor SL-20 (see Fig. 2); reef water level Δh refers to flight number 1, serving as reference case with $\Delta h = 0$ m; mean water depth $\overline{h}$ on the reef as average submergence of the irregular reef bottom within the study site.

Set:	**Ref.**	**S1**		**S2**		**S3**		**S4**		
Flight number:	**1**	**2**	**3**	**4**	**5**	**6**	**7**	**8**	**9**	**10**
Sea level z_{SL} [m]	-0.41	-0.19	-0.14	0.05	0.07	0.20	0.23	0.33	0.33	0.33
Reef water level Δh [m]	0.00	0.22	0.27	0.46	0.48	0.61	0.63	0.74	0.73	0.74
Mean water depth $\overline{h}$ [m]	0.02	0.07	0.09	0.19	0.21	0.30	0.33	0.42	0.41	0.41
Local survey time	11:35	12:50	13:10	14:20	14:30	15:15	15:30	16:45	17:00	17:30

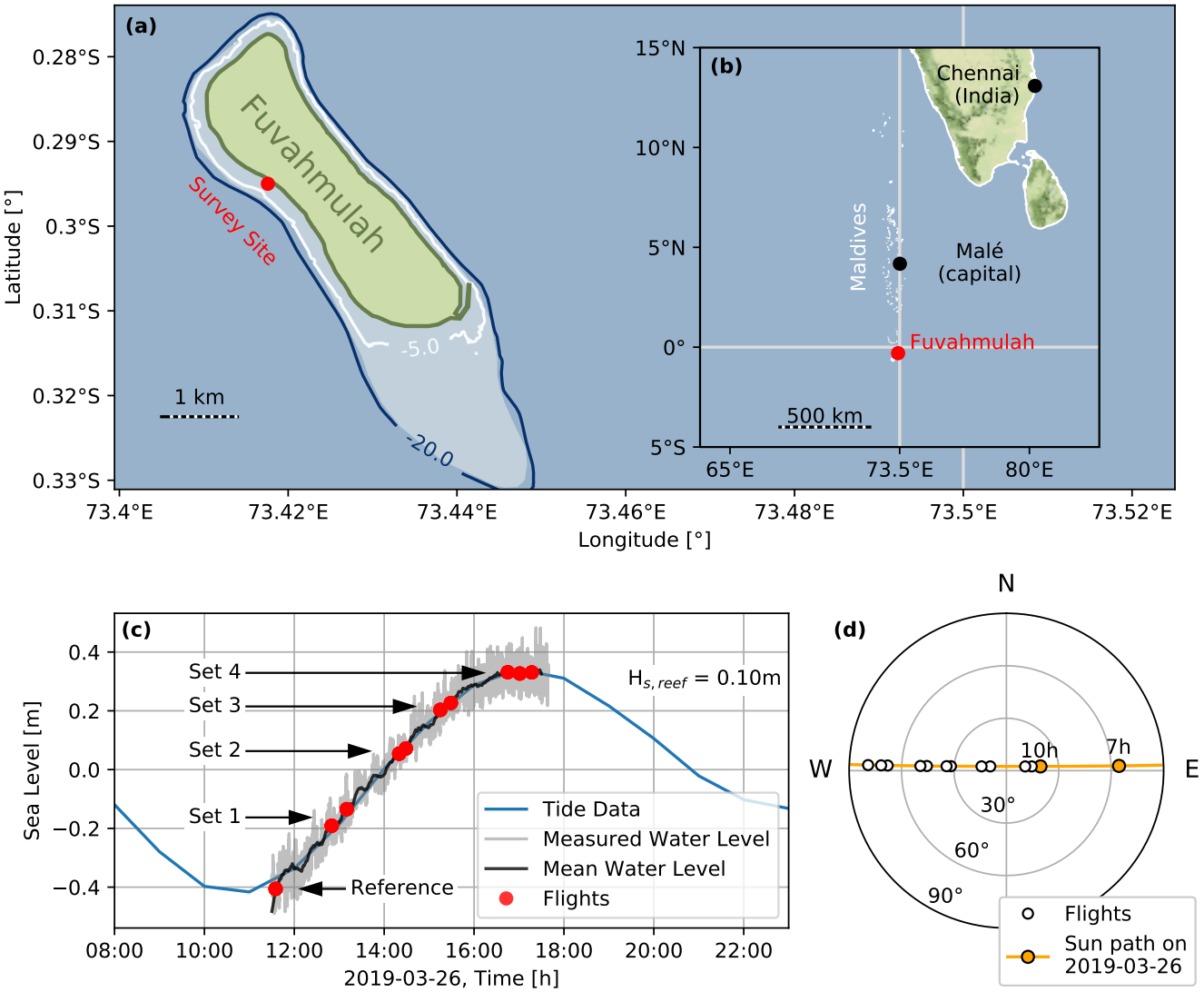

Figure 1. Geographic location and field conditions. Location of **(a)** the study site on the island and **(b)** of Fuvahmulah within the Indian Ocean; **(c)** displays the sea level for the survey based on nearby tide data and water levels measured on site. On March 26th, 2019, the measured data and mean significant wave height on the reef $H_{s,\mathrm{reef}}$ is recorded by wave gauge SL-20 (see Fig. 2); **(d)** sun position on March 26th, 2019 throughout the day (orange markers are exemplary times at 07:00 and 10:00 for orientation) at associated flight times (white marker, for exact times see Table 1).

of excavated rocks. The remaining reef flat on the left side consist of corals, sand and seagrass. On the landward side of the reef, seagrass grows on the corals and traps sand. Small ponds form in areas which lack seagrass and thus sand cover. These ponds remain submerged for the entire study.
The fringing reef attenuates incoming waves, but the area is still subject to water surface undulations. Sensor SL-20 (see Fig. 2) records the significant wave height – the sensor lies in the inundated channel and measures constantly throughout the entire field survey. The resulting significant wave height on the reef is $H_s = 0.10\,\mathrm{m}$, calculated as the mean of the highest 33 % waves from a zero-crossing analysis.

The survey site contains 12 uniquely colored and labeled GCPs. These GCPs are made of 0.5 m wide square PVC-tarpaulin sheets. Later, in the SfM-MVS process, the GCPs serve as georeference and scaling of the point cloud and they are used in the bundle adjustment to optimize the image alignment. Therefore, each GCP's center position

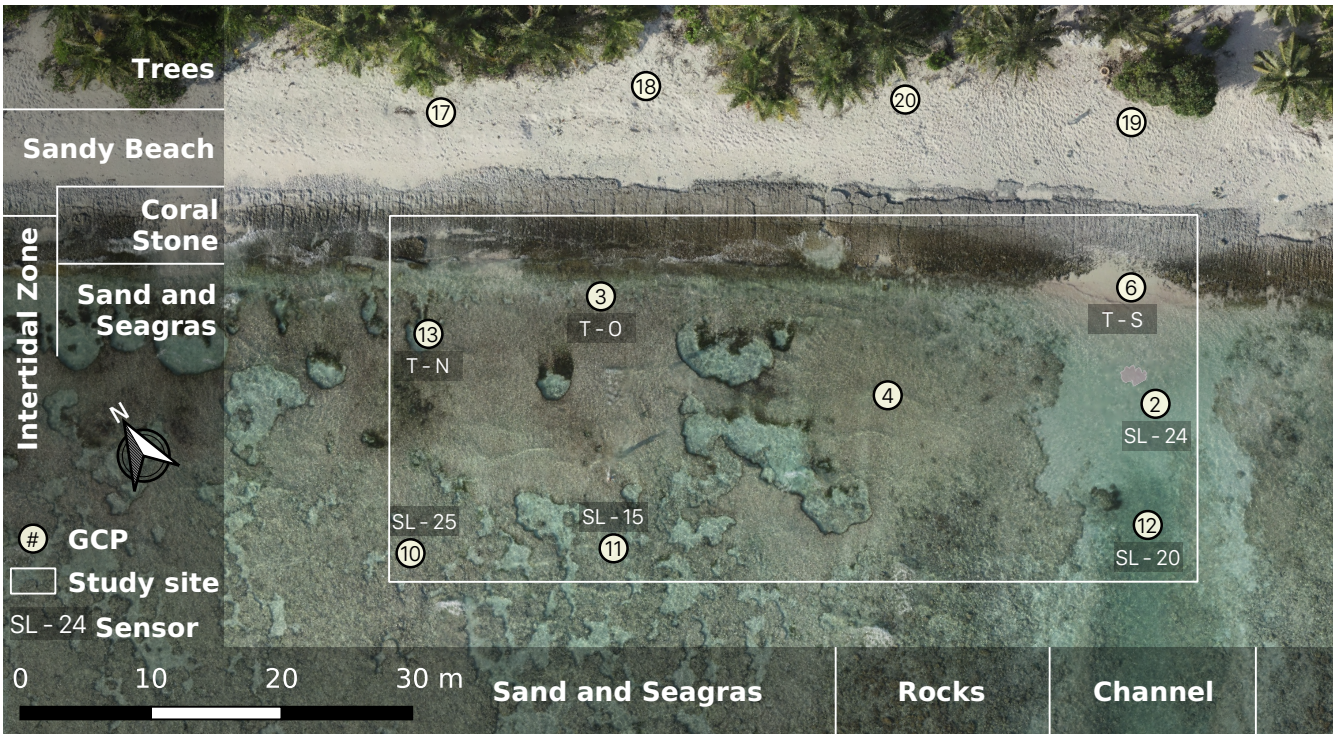

Figure 2. Survey site, study site and setup. Orthophoto of the survey site on the reef, with reef areas classified according to their landform. The white border shows the study site within the survey site. Round circles show the Ground Control Point (GCP) locations. GCPs paired with pressure sensores have a sensor identifier label next to them.

is measured with a survey grade GNSS system, being set up as base-rover combination for RTK measurements. Both GNSS devices are SEPTENTRIO ASTERX-U receiver combined with a NAVX-3G antenna. The devices measure the GCPs' position with an accuracy of 1.24 ± 0.14 cm. An equal distribution of GCPs further supports the alignment quality: four GCPs cover the constantly dry sandy beach, while the remaining eight GCPs lie on the shoreward half of the intertidal reef flat. Seven of the eight reef GCPs are also paired with pressure sensors, measuring the water depth constantly (see Fig. 2). The sampling rate is between 1 Hz and 8 Hz for the four Seametrics PT2X sensors (ID: SL-*number*, in Fig. 2) and 16 Hz for the three DRIESSEN + KERN P-Log3021-MMC sensors (ID: T-*letter*, in Fig. 2). Additionally, the water depths are measured manually with a folding rule at the start of each flight. The mean water depth $\overline{h}$ is the averaged water depth on the reef during each flight, considering all pressure sensors. In this study, all water depths are measured on-site, while water levels are based on tide data from University of Hawai'i Sea-Level Center (UHSLC) (Caldwell et al., 2015).

Digital Elevation Models

A DJI Phantom 4 Pro (V.1) quadcopter records aerial images in ten flights with 25 m altitude from the take-off location. Each flight is considered one survey, as every flight covers the entire survey area. Flight planning is done by DRONEDEPLOY, allowing to record images automatically every 2 s. To record the images, the drone carries a 20 megapixel camera with the camera angle at nadir position (perpendicular to the ground). Therefore, images overlap 80 % in the front and 75 % on the sides. To further improve three-dimensional reconstruction, all surveys – except number four to six – also contain images around the survey area in non-nadir position (DRONEDEPLOY option *3D Mode* turned on). While the first flight of the entire study is the reference flight over the dry reef, all other flights are clustered in four sets with two flights each – except for the last set containing three flights. Repeating flights in each set with similar boundary conditions creates redundancy and is meant to compensate for complications, such as deteriorated visibility. The time between the start of each set is about 45 min to 75 min, while within each set, the time between the take-offs is 10 min to 20 min (see Fig. 1c).

The aerial images of each flight are the basis for a three dimensional reconstruction, being carried out with METASHAPE (v1.5.3 Professional, build 8432; Agisoft.com), a commercial, proprietary software solution by AGISOFT LLC (Agisoft, 2019) incorporating Structure-from-Motion (SfM) (Westoby et al., 2012) and MVS algorithms (in the following referred to as SfM-MVS). The software uses the recorded aerial images of each flight to find clearly distinguishable points in two or more images (tie points; with SfM-MVS). Based on these points, METASHAPE aligns the cameras. Afterwards the software uses the aligned aerial images to calculate a dense point cloud (with MVS) and then creates three-dimensional models, serving as base for the DEMs and orthophotos. This procedure is carried out for each flight (see Table 1), resulting in 10 models. In this study the DEMs of each model have a resolution of $1.36\,\mathrm{cm\,px^{-1}}$ to $1.76\,\mathrm{cm\,px^{-1}}$ and the associated orthophotos have a resolution of $0.68\,\mathrm{cm\,px^{-1}}$ to $1.31\,\mathrm{cm\,px^{-1}}$. The quality setting for each reconstruction step in METASHAPE are set to high (see supplementary materials for further information on settings in METASHAPE). Images taken with off-nadir camera orientation prevent systematic vertical errors in the photogrammetric processes, usually refered to as *"doming"* (James and Robson, 2014; Casella et al., 2020). The photogrammetric reconstruction of the reef from images of flight 4 leads to visible doming and will not be considered in the further evaluation.

The first flight captures the dry reef and serves as reference case for all following flights. All following flights will record the site under rising tide and thus higher water levels. Acknowledging deviations between coordinates in DEMs and independent measurements (Casella et al., 2020), in this study the dry reef's DEM is the most exact reconstruction of the reef. Therefore, the resulting deviation DEM (ΔDEM) describes the error made by the SfM-MVS algorithm in underwater areas:

$$\Delta\mathrm{DEM}_i = \mathrm{DEM}_{\mathrm{surface},1} - \mathrm{DEM}_{\mathrm{inundated},i} \tag{1}$$

with the dry reference $\mathrm{DEM}_{\mathrm{surface},1}$ of flight 1, the gradually inundated topographies $\mathrm{DEM}_{\mathrm{inundated,i}}$, and index i for flights 2 to 10 (see Table 1). Consequently, calculating the deviation between the dry reference DEM and those from an increasingly inundated area reveals the ability of the SfM-MVS algorithm to reconstruct underwater topography

for different water levels. With regard to ΔDEM, negative values mean the SfM-MVS algorithm considers the area to be shallower than the actual dry topography and vice-versa positive values show deeper waters.

We consider two survey methods, that have an impact on the alignment procedure in the photogrammetric process:

(a) The first approach considers the area of interest to be fully accessible and uses all available – even submerged – GCPs in the alignment.

(b) The second approach is done by assuming that only dry areas were accessible, disregarding the submerged GCPs no.12 in the channel and no. 13 lying in a pond. As the water level increases, GCPs becoming wet are also neglected in the associated alignment (for more information, see supplementary materials).

Furthermore, we also present two different approaches to analyze the error made by the SfM-MVS algorithm in underwater areas:
The first method illustrates the rastered ΔDEMs over the reference flight's orthophoto, giving a more straightforward overview of the reconstruction error for each survey and it's associated reef water level Δh separately (Fig. 3).
Another, more integral approach considers the data of all surveys at once: Since ΔDEM indicates the error made by the SfM-MVS algorithm in underwater areas, pairing the error e_{px} of each pixel in ΔDEM with the pixel's water depth h_{px} yields a water depth-dependent representation of the reconstruction error (carried out in PYTHON v.3.7.4 with the modules RASTERIO v.1.1.3 and FIONA v.1.8.13 post). Here, the water depth at each pixel h_{px} is derived from the mean water depth on the reef $\overline{h}$ for each flight (see Table 1).
Combining the data from all nine ΔDEMs results in about $2-3\cdot10^7$ data points. To illustrate this sheer amount of point data, two-dimensional histograms analyze the error occurrence probability over water depth (Fig. 4 and 5 in results). These two dimensional histograms employ a 5 mm by 1 mm raster (h_{px} by e_{px}), yielding 1.1 million combinations of h_{px} and e_{px} (python module: MATPLOTLIB, v3.1.3 with function *hist2d*). The according mean elevation difference $\overline{e}$ combines all e_{px} in one water depth h-bin of the histogram as

$$\overline{e} = \frac{1}{N_h}\sum_{n=1}^{N_h} e_{\mathrm{px},n} \tag{2}$$

with N_h as number of e_{px} per h-bin of the histogram. Based on the two dimensional histograms, a regression function of $\overline{e}$ summarizes the mean error as function of the water depth h, hence giving a general water depth-dependent error estimate for photogrammetric reconstruction of inundated areas:

$$\mu(h) = y + \sum_{o=1}^{\mathscr{O}} m_o \cdot h^o \tag{3}$$

with $\mathscr{O}$ as order of the regression function, m_o as estimated coefficients for the regression problem and y as the function's intercept of the ordinate (python module: SCIKIT-LEARN v0.21.3, with *LinearRegression* function for $\mathscr{O}=1$ and *PolynomialFeatures* function for $\mathscr{O}>1$). The coefficient of determination R^2 expresses the regression function's quality to approximate the measured mean elevation difference $\overline{e}$:

$$R^2 = 1 - \frac{\sum_{n=1}^{B_h}(\overline{e}_b - \mu(h)_b)^2}{\sum_{b=1}^{B_h}(\overline{e}_b - \overline{\overline{e}})^2} \tag{4}$$

with B_h as number of bins, $\overline{e}_b$ as true value $\overline{e}$ in each bin b and $\mu(h)_b$ as the predicted value of $\overline{e}_b$ using the water depth h in the regression function (Eq. 3). If $R^2=1$, the regression function predicts the mean elevation difference $\overline{e}$ perfectly. R^2 decreases when the relationship worsens and if R^2 is negative, the regression function predicts $\overline{e}_b$ less accurate than $\overline{\overline{e}}$, (with $\overline{\overline{e}}$ as the mean of $\overline{e}$, calculated analogously to Eq. 2 for all bins b of B_h. The *R^2score*

function comes from the python module SCIKIT-LEARN version 0.21.3). In this study, the regression functions are valid between the water depth limits $h = 5\,\text{cm}$ and $h = 73\,\text{cm}$. The lower end is defined by the amplitude a of the significant wave height with $a = 0.5H_s$, while the upper end correlates to the maximum water level on the reef Δh_{max} (see Table 1). The root mean square error RMSE between the regression function and the each pixel's elevation difference e_{px} from the survey is

$$\text{RMSE} = \sqrt{\frac{1}{N_{px}-1}\sum_{n=1}^{N_{px}}\left(e_{\text{px}} - \mu(h_{\text{px}})\right)^2} \tag{5}$$

with N_{px} as all considered pixels from every ΔDEMs (python module: SCIKIT-LEARN with *mean_squared_error* function and option $squared = False$).

Refraction correction

Snell's law describes the main challenge and error source of airborne SfM-MVS to reconstruct bathymetry: a submerged object reflects light, traveling to the camera which then records the optical information in an aerial image. However, as the light travels through two media, it refracts at the water surface, altering how inundated areas appear on the image (Woodget et al., 2015; Dietrich, 2017). Snell's law is the mathematical description of underwater objects, appearing to be shallower from outside the water:

$$n_1 \sin(i) = n_2 \sin(r) \tag{6}$$

with n_1 as refractive index of water (1.337 for fresh water in Dietrich, 2017), n_2 as refractive index of air (1.0 in Dietrich, 2017), i as incident- and r as refraction angle (nadir to SfM-MVS point). Snell's equation accounts for the systematic underprediction of water depths in airborne imagery. Therefore, recent studies used Eq. 6 and presented attempts correcting optical refraction and improving SfM-MVS in underwater areas (Woodget et al., 2015; Dietrich, 2017; Chirayath and Instrella, 2019). For example, the PYTHON-based, open-source algorithm PY_SFM_DEPTH (Dietrich, 2017) builds on existing approaches (Woodget et al., 2015), provides an additional processing step to METASHAPE, and avoids extra costs by special lensing systems (as for example in Chirayath and Instrella, 2019). The algorithm reverse-engineers the vertical underwater position of the submerged dense points by applying Snell's law on the point's apparent locations. To achieve this, PY_SFM_DEPTH uses the information of each point's cameras (location and orientation) as well as an interpolated, plain water level – similar to the calculation of h_{px} in this study. PY_SFM_DEPTH is designed for shallow and calm inland waters without using underwater GCPs to align the point cloud (Dietrich, 2017). According to the homepage of PY_SFM_DEPTH, the refraction correction provides the best outcome with clear water, as few as possible reflections, and minimal water surface ondulations (Dietrich, 2020). The homepage also predicts that waves will *"increase the 'noise' in the SFM point cloud ...* [and] *lead to inaccuracies/errors in the final outputs"*. With this in mind, the present study tests the refraction correction algorithm PY_SFM_DEPTH for coastal waters under site specific wave impact with aerial images from flights 6 and 10 (with mean reef water depths Δh of 0.61 m and 0.74 m, see Table 1). The resulting two dimensional histograms are based on about $4.4 - 4.5 \cdot 10^6$ data points (Fig. 5).

Results

As outlined in the methods, this study tests two survey approaches: in the first approach, the reef is accessible and underwater GCPs can be recorded. In the second approach, only the dry areas are considered to be accessible and thus submerged GCPs are not considered in the photogrammetric procedure. The next section presents results from the native workflow with METASHAPE – both with and without refraction corrected depths. The following section contains the same procedure with refraction corrected models.

Bathymetric reconstruction with submerged and dry Ground Control Points

The first analysis of bathymetric reconstruction assumes that the reef is accessible and underwater GCPs can be recorded. Here, the SfM-MVS algorithm uses all GCPs in the alignment step of the reconstruction, including inundated GCPs. The result is the orthophoto of the reference, dry topography, combined with data from all ΔDEMs (see Fig. 3). The ΔDEMs contain the differences between the dry and submerged reef from two of the ten flights. Following Snell's Law (Eq 6), negative values imply the actual, dry reef $DEM_{surface}$ being lower than appearing on the submerged $DEM_{inundated,i}$ and vice versa for positive values. In general, the results confirm the suggested deviation and underpredicted water depths of submerged areas. Also, the largest differences between the reconstructions of the dry and wet reef occurs in the deeper channel on the right side. Especially for areas subject to more hydrodynamic activity – especially breaking waves – the SfM-MVS algorithm does not always find matching points, resulting in no-data patches (white areas in Fig. 3b and c).

However, the central area of the study site stands in contrast to the general results: The water depth in the shallower area of the DEM is overestimated when not or only slightly submerged ($\Delta h = 0.274\,\mathrm{m}$ and $0.633\,\mathrm{m}$, Fig. 3a and b). This area is slightly shallower than the adjacent areas on the left (see photos in supplementary materials). Some rocky outcrops remain above the water level and defining a definite coastline is difficult in this area (see Fig. 3a). But even the DEM with the highest submergence (Fig. 3c) still contains eventual, small spots being overpredicted, albeit all rocky outcrops are submerged. Also, the area above the channel is constantly overestimated for all submergence levels. These results show that the SfM-MVS algorithm forces the submerged areas to match the inundated GCPs, negatively affecting adjacent dry areas.

The results from the orthophotos only give insights into each particular flight. Calculating the specific water depth of each pixel and combining it with the measured difference of water depth, gives an integrated view over all flights. This method presents the SfM-MVS algorithm's performance to reconstruct underwater areas. The test case using submerged GCPs in the alignment phase results in $30.5 \cdot 10^6$ data points, facilitating a probabilistic estimation of errors (see Fig. 4). For water depths h between 0.05 m to 0.73 m the bathymetry is increasingly overestimated by a rate of $-13.2 \pm 21.7\,\%$ of the water depth (see Fig. 4a). The corresponding linear function of

$$\mu(h) = -0.132h + 0.017 \tag{7}$$

describes this trend with the water depth h and a root mean square error of $\mathrm{RMSE} = 0.008\,\mathrm{m}$ ($R^2 = 0.91$).

If the submerged reef was not accessible, only dry surface GCPs could be used in the alignment. This prevents the SfM-MVS algorithm to force the submerged areas on the GCPs. As the water level increases, the number of GCPs available for aligning decreases. Therefore – and as expected from Snell's Law (Eq. 6) – the underwater reconstruction for this approach is less accurate and the errors increase to $-35.2 \pm 13.9\,\%$ of the water depth for this study (see Fig. 4b, based on $19.9 \cdot 10^6$ points). The linear function of the regression analysis is

$$\mu(h) = -0.352h + 0.104 \tag{8}$$

The function yields a root mean square error of $\mathrm{RMSE} = 0.030\,\mathrm{m}$ between 0.05 m to 0.73 m water depth ($R^2 = 0.86$).

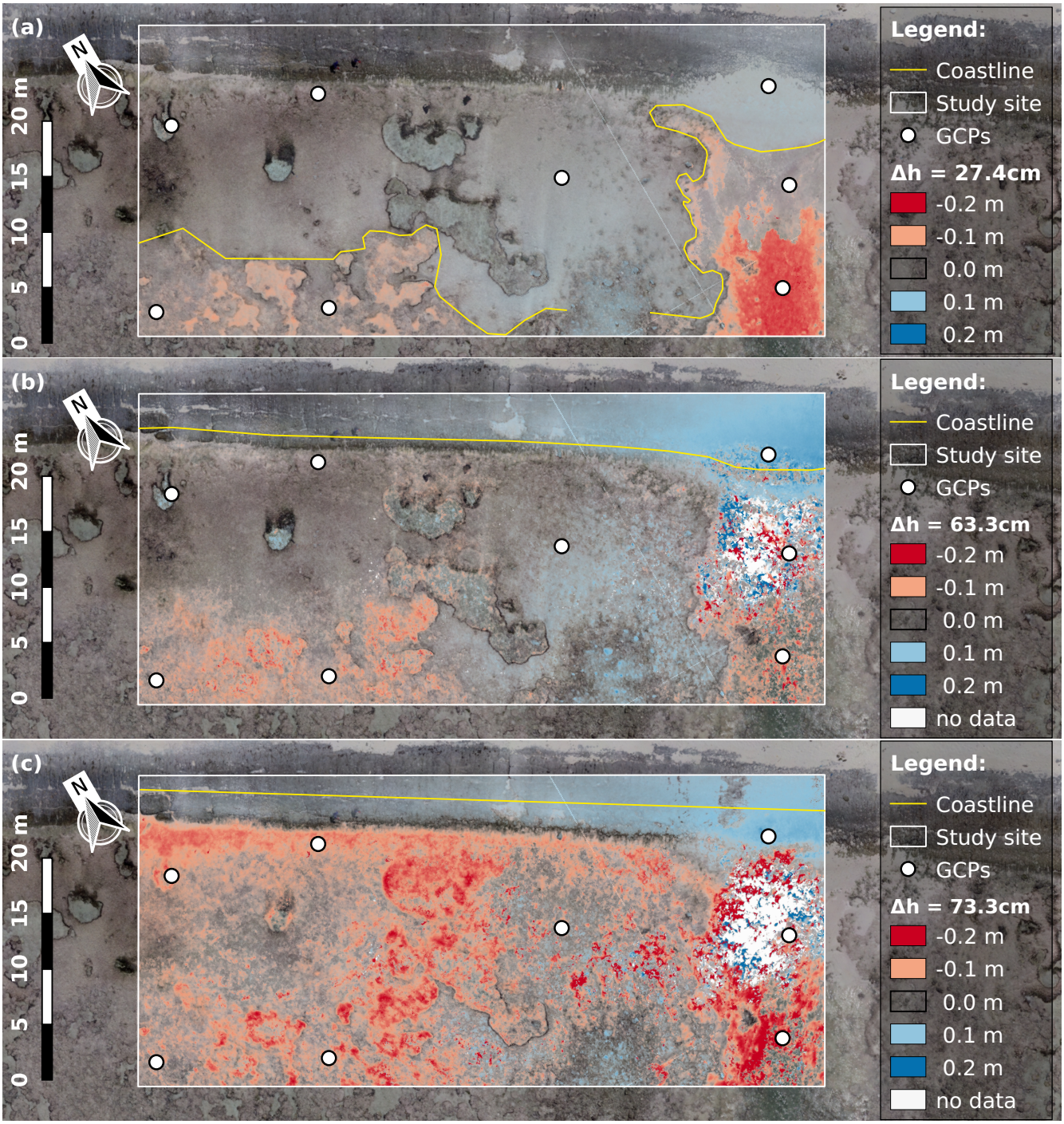

Figure 3. ΔDEMs for flight 3, 7 and 9. Difference between the initial, dry DEM and **(a)** the submerged DEMs with $\Delta h = 0.274\,\text{m}$ (flight 3), **(b)** $\Delta h = 0.633\,\text{m}$ (flight 7), and **(c)** $\Delta h = 0.733\,\text{m}$ (flight 9) in the study area. Difference values range between $\pm 20\,\text{cm}$, the yellow lines are the coastlines, manually extracted from orthophotos and aerial images (see supplementary materials).

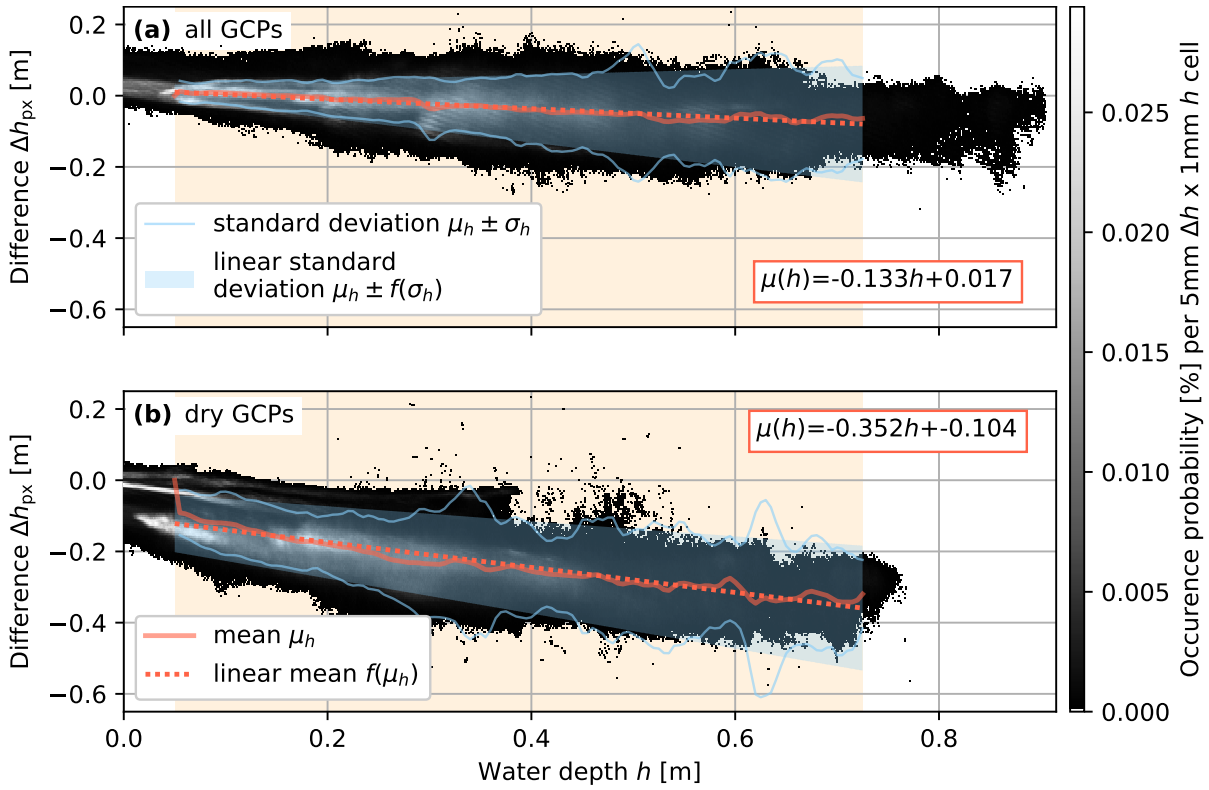

Figure 4. Performance of underwater reconstruction. The Fig. combines the occurrence probability of depth differences e_{px} between the reference DEM and the submerged DEMs with the associated water depths h in the study area. **(a)** illustrates the results for DEMs being aligned with all GCPs and **(b)** with DEMs considering only surface ("dry") GCPs. A linear regression $\mathcal{O} = 1$ for each case summarizes the scatter plots by giving a function $\mu(h)$ of the mean deviation in dependence of the depth. The function is valid in the range of 0.05 m to 0.73 m.

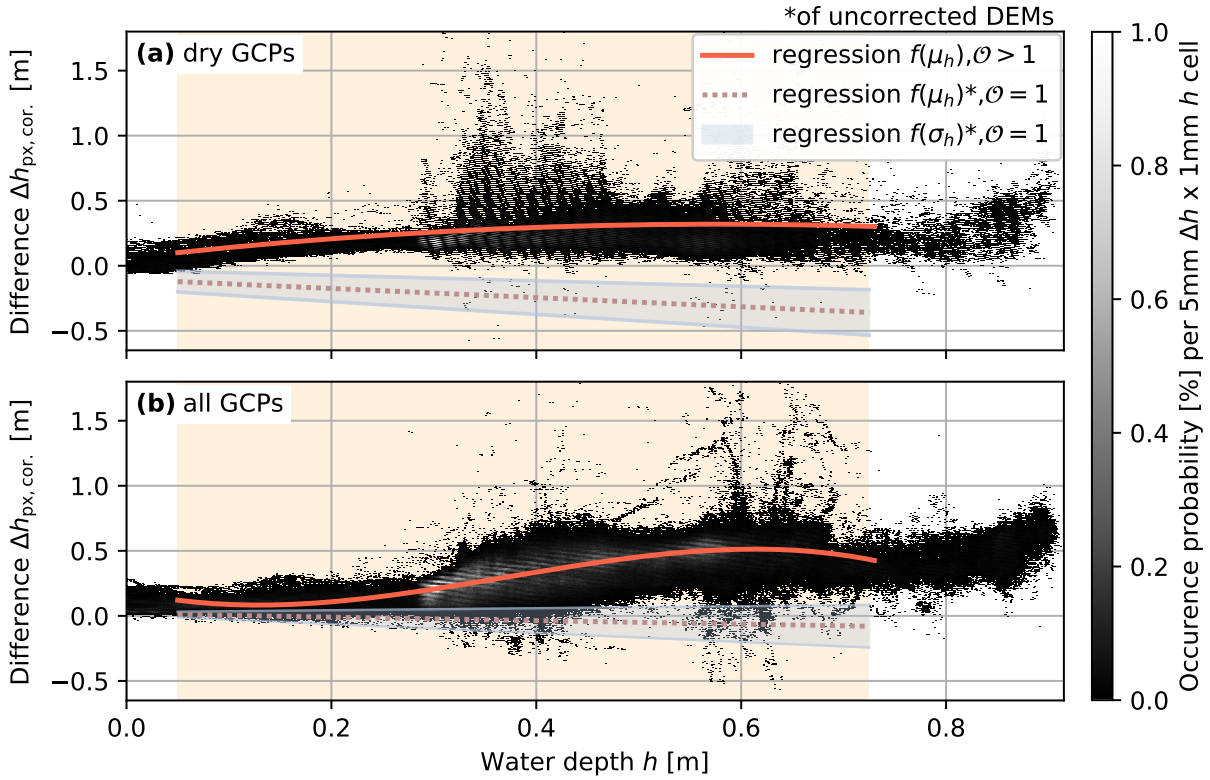

Figure 5. Performance of underwater reconstruction with refraction correction. The Fig. combines the occurrence probability of depth differences $e_{\text{px,corr}}$ between the reference DEM and the refraction corrected, submerged DEMs with the associated water depths h in the study area. **(a)** illustrates the results for DEMs being only aligned with dry surface GCPs and **(b)** with DEMs considering all GCPs. The scatter plots of the refraction corrected DEMs are best summarized by higher order regression functions $\mu(h)$ with $\mathcal{O} > 1$. The results are plotted against the linear regression with $\mathcal{O} = 1$ from Fig. 4a to visualize the error scale compared to the uncorrected reconstruction. The functions are valid in the range of 0.05 m to 0.73 m.

Refraction correction

Recent attempts successfully corrected water depths from aerial images in riverine environments (Westaway et al., 2000; Woodget et al., 2015), for example with an additional processing step after the alignment (Dietrich, 2017). Comparing the corrected with the uncorrected DEMs and using only surface GCPs shows an inverse behavior between the uncorrected and the corrected reconstruction errors: with the refraction correction applied, the error is now positive, meaning the correction reconstructs the inundated areas deeper than they are in the reference DEM (Fig. 5a, based on $4.4 \cdot 10^6$ points). The regression analysis approximates the performance with the function

$$\mu(h) = -0.805h^2 + 0.921h + 0.056. \tag{9}$$

The function yields a root mean square error of RMSE $= 0.271$ m for water depths h between 0.05 m to 0.73 m ($R^2 = 0.84$). The relatively constant error of below 0.5 m (see Fig. 5) is in accordance with the method's expected error of 0.02 % of the flying altitude (Dietrich, 2017).

Regarding the absolute error of the reconstruction with underwater GCPs and of the refraction corrected reconstruction without GCPs (Fig. 4a and 5a), both methods perform about equally well for water depths between 0.10 m to 0.55 m. Beyond depths of 0.55 m the error by the refraction correction stabilizes, while it increases for the uncorrected DEMs. Therefore, despite subject to sub-par field conditions, the bathymetric reconstruction benefits from the refraction correction in deeper waters, when no underwater GCPs are used. However, the SfM-MVS

algorithm still aligns the bathymetry more exactly with submerged GCPs than correcting an unaligned bathymetry. In contrast, correcting DEMs aligned with underwater GCPs is detrimental (Fig. 5b, based on $4.5 \cdot 10^6$ points). This further increases the error when compared to refraction corrected DEMs using only dry GCPs. The regression analysis approximates the increased error with the function

$$\mu(h) = 1.705h^3 - 2.802h^2 - 1.581h + 0.001 \tag{10}$$

The function is valid in the range of 0.05 m to 0.73 m with a RMSE of 0.194 m ($R^2 = 0.98$).

Discussion & Conclusion

In photogrammetry, when light refracts on the water surface, submerged objects appear distorted on airborne images, leading to falsely estimated water depths in SfM-MVS algorithms. This study quantifies these errors with data from a specially designed field experiment. Our results show the SfM-MVS algorithm underestimates underwater areas by $13.2 \pm 21.7\,\%$ (see Fig. 4) of the water depth when submerged GCPs are used in the optimization process. But reconstruction accuracy of adjacent surface areas decreases with this method. Without using submerged GCPs in the optimisation process, the error is at $35.2 \pm 13.9\,\%$ of the water depths and the reconstruction benefits from refraction correction in waters deeper than 0.55 m.
In our example, the uncorrected reconstruction leads to underestimated water depths while the corrected reconstruction overestimated the submergence. Despite a varying order $\mathcal{O}$ in the approximation of the error function $\mu(h)$ (see Eq. 3 as well as Fig. 4 and 5), future studies should clarify if the reconstruction for water depths up to ≈ 1 m in general benefit from combining the corrected and uncorrected approach. However, beyond water depths of ≈ 1 m, the uncorrected reconstruction would impair the refraction correction's relatively stable performance in deeper waters (Fig. 5).

Comparing airborne photogrammetry with other methods to obtain bathymetries (for example LiDAR, echosounder, etc.) reveals that SfM-MVS algorithms provide good estimates of water depth as well as mapping abilities for clear waters with low hydrodynamic activity. This study however uses the approach in more challenging environments and utilizes data recorded under field conditions: The survey was carried out on a sunny day with low winds, which can be considered normal for the late dry-season in the Maldives. Also, the off-shore wave height H_s of 0.88 m to 1.00 m is normal for Fuvahmulah in March, albeit lower than average (David and Schlurmann, 2020). The fringing reef attenuates these waves, but the study site still experiences hydrodynamic activity – for example in form of bores, surges, associated wave run-up etc. (Monismith, 2007) – which increase as the tide rises. The statistical zero-crossing method used here to calculate H_s does not consider the smaller surface waves traveling on ondular bores (Sous et al., 2019) but represent the sea state reasonably well compared to qualitative observations on site. Still, waves in the study area affect the results in several aspects:

- Reconstructing underwater scenes suffers from light refraction on the plain water surface (Casella et al., 2016; Dietrich, 2017). If the water surface changes while recording, the incident and reflection angle change in Snell's Law. As consequence, the SfM-MVS and MVS algorithms get ambiguous information on an object's location and shape and can fail to give any information for these areas (see *no data* areas in Fig. 3).

- Ambiguous information impacts the refraction correction even stronger than SfM and MVS, since it relies on camera position and orientation to emend the appearing depth to the actual depth of each underwater dense point. The ambiguity results in more noise (as described in the manual of PY_SFM_DEPTH). This underlines that the refraction correction highly depends on calm waters to improve mapping of submerged structures. However, even with waves present, it still benefits the bathymetric reconstruction without underwater GCPs.

- Water surface undulations also impact the mean water level estimation, used to calculate the water depth h of each pixel in ΔDEM, as well as for the refraction correction. Both use an averaged water level derived from the all measurements in the study site, neglecting the spatio-temporal variation of h within each flight (compare water levels Δh at sensor SL-20, Table 1). In absence of water level measurements, the plain water level for the refraction correction could be estimated by sampling the water edge on a river's bank (Dietrich, 2020). However, this post-processing step is less accurate on beaches, because they experience wave run-up. With wave run-up, the coastline is varying and therefore, manual water edge or coastline detection is more difficult and somewhat more arbitrary in coastal areas.

In summary, the appropriate approach for bathymetry reconstruction and mapping of underwater areas depends on the desired outcome (see Table 2). However, among the discussed alternatives, airborne photogrammetry with user-grade equipment yields both good bathymetric reconstruction and aerial mapping of shallowly inundated areas, albeit the reconstruction error increases with water depth. Quantifying the depth-dependent error in a typical field

campaign environment encourages to extent surface ("dry") beach surveys with conventional UAVs beyond the coastline. The reconstruction benefits from adapting aligning strategies and – beyond a depth of 0.55 m – from refraction correction on reef platforms under typical wave conditions.

Table 2. Bathymetric drone surveys in literature and results of this study.

Study	Water depth	Difference	Deviation	Notes
Westaway et al., 2000	$< 0.6\,\mathrm{m}$	$0.04\,\mathrm{m} - 0.10\,\mathrm{m}$	$\pm 0.09\,\mathrm{m} - 0.15\,\mathrm{m}$	refraction correction, riverine
Casella et al., 2016	$< 1.8\,\mathrm{m}$	$0.02\,\mathrm{m}$	$\pm 0.45\,\mathrm{m}$	native, reef areas
Woodget et al., 2015	$< 0.14\,\mathrm{m} - 0.18\,\mathrm{m}$	$0.01\,\mathrm{m} - 0.05\,\mathrm{m}$		refraction correction, riverine
Dietrich, 2017	$< 1.8\,\mathrm{m}$	0.02 % flying altitude		refraction correction, riverine (code: PY_SFM_DEPTH)
Casella et al., 2020	only surface	0.005 m to 0.21 m		dry beaches, literature overview
This study	$< 0.74\,\mathrm{m}$	0.13 % water depth		with underwater GCPs, reef
		0.35 % water depth		no underwater GCPs, reef
		0.02 % flying altitude		refraction correction, reef

Acknowledgments

This study took place in the project "Dealing with change in SIDS: societal action and political reaction in sea level change adaptation in Small Island Developing States (DICES)", grant no. SCHL 503/17-1 (CGD, NK, PB, TS) and "Holocene sea-level changes in Southeast Asia (SEASchange)", grant no. RO-5245/1-1 (AR). The projects are framed within the priority programm (SPP-1889) - regional sea level change and society of the German Research Foundation (Deutsche Forschungsgemeinschaft, DFG). Elisa Casella acknowledges the Leibniz Center for Tropical Marine Research for economical support.
The authors would like to thank Ali Ahmed, Tatiana Ivanova, René Klein, Ibrahim Shiyan (Panda), Zahid as well as Marion and Uwe Zander for their help in the field campaigns. On the Maldives, the authors were supported by the Maldives Meteorological Service (MMS), Fuvahmulah Island Council and Fuvahmulah DIVE School. The authors would also like to thank James T. Dietrich for feedack on his refraction correction routine.

Author Contribution Statement

CGD planned the survey with input from EC and AR. PB and AR prepared the devices. PB provided the data from the hydrodynamic measurements. CGD, NK and PB carried out the field campaign. CGD and NK post-processed the data with help and advice from EC and AR. CGD prepared the manuscript with help of NK. EC, AR and TS edited and contributed to the final manuscript. AR and TS designed the research projects in the research program, funding this study.

Conflict of interest

The authors declare that they have no conflict of interest.

References

Agisoft (2019). *Agisoft Metashape User Manual: Professional Edition, Version 1.5*. agisoft.com/pdf/metashape-pro_1_5_en.pdf.

Bandini, F., Olesen, D., Jakobsen, J., Kittel, C. M. M., Wang, S., Garcia, M., and Bauer-Gottwein, P. (2018). Technical note: Bathymetry observations of inland water bodies using a tethered single-beam sonar controlled by an unmanned aerial vehicle. *Hydrology and Earth System Sciences*, 22(8):4165–4181.

C3S (2017). ERA5: Fifth generation of ECMWF atmospheric reanalyses of the global climate by the Copernicus Climate Change Service (C3S). https://cds.climate.copernicus.eu/cdsapp#!/home. Copernicus Climate Change Service Climate Data Store (CDS). Last date of access: 2020-05-31.

Caldwell, P. C., Merrifield, M. A., and Thompson, P. R. (2015). Sea level measured by tide gauges from global oceans — the joint archive for sea level holdings (ncei accession 0019568). Dataset. Version 5.5, NOAA National Centers for Environmental Information,.

Carrivick, J. L., Smith, M. W., and Quincey, D. J. (2016). *Structure from Motion in the Geosciences*. John Wiley & Sons, Ltd.

Casella, E., Collin, A., Harris, D., Ferse, S., Bejarano, S., Parravicini, V., Hench, J. L., and Rovere, A. (2016). Mapping coral reefs using consumer-grade drones and structure from motion photogrammetry techniques. *Coral Reefs*, 36(1):269–275.

Casella, E., Drechsel, J., Winter, C., Benninghoff, M., and Rovere, A. (2020). Accuracy of sand beach topography surveying by drones and photogrammetry. *Geo-Marine Letters*, 40(2):255–268.

Chirayath, V. and Instrella, R. (2019). Fluid lensing and machine learning for centimeter-resolution airborne assessment of coral reefs in American Samoa. *Remote Sensing of Environment*, 235:111475.

Colbo, K., Ross, T., Brown, C., and Weber, T. (2014). A review of oceanographic applications of water column data from multibeam echosounders. *Estuarine, Coastal and Shelf Science*, 145:41 – 56.

Costanza, R., De Groot, R., Sutton, P., Van der Ploeg, S., Anderson, S. J., Kubiszewski, I., Farber, S., and Turner, R. K. (2014). Changes in the global value of ecosystem services. *Global environmental change*, 26:152–158.

David, C. G. and Schlurmann, T. (2020). Hydrodynamic drivers and morphological responses on small coral islands – The Thoondu spit in Fuvahmulah, the Maldives (Provisionally accepted). *Frontiers in Marine Sciences*.

Dietrich, J. T. (2017). Bathymetric Structure-from-Motion: extracting shallow stream bathymetry from multi-view stereo photogrammetry. *Earth Surface Processes and Landforms*, 42(2):355–364.

Dietrich, J. T. (2020). py_sfm_depth homepage. geojames.github.io/py_sfm_depth/. Last accessed: June 3rd, 2020.

Duvat, V. K. E. and Magnan, A. K. (2019). Rapid human-driven undermining of atoll island capacity to adjust to ocean climate-related pressures. *Scientific Reports*, 9(1).

Ferrario, F., Beck, M. W., Storlazzi, C. D., Micheli, F., Shepard, C. C., and Airoldi, L. (2014). The effectiveness of coral reefs for coastal hazard risk reduction and adaptation. *Nature Communications*, 5(1).

Fine, M., Hoegh-Guldberg, O., Meroz-Fine, E., and Dove, S. (2019). Ecological changes over 90 years at low isles on the great barrier reef. *Nature Communications*, 10(1).

Hedley, J. D., Roelfsema, C., Brando, V., Giardino, C., Kutser, T., Phinn, S., Mumby, P. J., Barrilero, O., Laporte, J., and Koetz, B. (2018). Coral reef applications of sentinel-2: Coverage, characteristics, bathymetry and benthic mapping with comparison to landsat 8. *Remote Sensing of Environment*, 216:598 – 614.

Hédouin, L., Rouzé, H., Berthe, C., Perez-Rosales, G., Martinez, E., Chancerelle, Y., Galand, P. E., Lerouvreur, F., Nugues, M. M., Pochon, X., Siu, G., Steneck, R., and Planes, S. (2020). Contrasting patterns of mortality in polynesian coral reefs following the third global coral bleaching event in 2016. *Coral Reefs*, 39(4):939–952.

Holmgren, W., Hansen, C., and Mikofski, M. (2018). pvlib python: a python package for modeling solar energy systems. *Journal of Open Source Software*, 3(29):884.

James, M. R. and Robson, S. (2014). Mitigating systematic error in topographic models derived from uav and ground-based image networks. *Earth Surface Processes and Landforms*, 39(10):1413–1420.

Kench, P. S. and Brander, R. W. (2006). Response of reef island shorelines to seasonal climate oscillations: South maalhosmadulu atoll, maldives. *Journal of Geophysical Research: Earth Surface*, 111(F1).

Klemas, V. (2011). Beach Profiling and LIDAR Bathymetry: An Overview with Case Studies. *Journal of Coastal Research*, 27(6):1019 – 1028.

Leon, J., Roelfsema, C. M., Saunders, M. I., and Phinn, S. R. (2015). Measuring coral reef terrain roughness using 'structure-from-motion' close-range photogrammetry. *Geomorphology*, 242:21 – 28. Geomorphology in the Geocomputing Landscape: GIS, DEMs, Spatial Analysis and statistics.

Mandlburger, G. (2019). Through-water dense image matching for shallow water bathymetry. *Photogrammetric Engineering & Remote Sensing*, 85(6):445–455.

Mandlburger, G., Pfennigbauer, M., Schwarz, R., Flöry, S., and Nussbaumer, L. (2020). Concept and performance evaluation of a novel UAV-borne topo-bathymetric LiDAR sensor. *Remote Sensing*, 12(6):986.

Monismith, S. G. (2007). Hydrodynamics of coral reefs. *Annual Review of Fluid Mechanics*, 39(1):37–55.

Murfitt, S. L., Allan, B. M., Bellgrove, A., Rattray, A., Young, M. A., and Ierodiaconou, D. (2017). Applications of unmanned aerial vehicles in intertidal reef monitoring. *Scientific Reports*, 7(1).

Panagou, T., Oikonomou, E., Hasiotis, T., and Velegrakis, A. F. (2020). Shallow water bathymetry derived from green wavelength terrestrial laser scanner. *Marine Geodesy*, 0(0):1–21.

Ratter, B., Hennig, A., and Zahid (2019). Challenges for shared responsibility – Political and social framing of coastal protection transformation in the Maldives. *DIE ERDE - Journal of the Geographical Society of Berlin*, 150(3):169–183.

Skirving, W. J., Heron, S. F., Marsh, B. L., Liu, G., Cour, J. L. D. L., Geiger, E. F., and Eakin, C. M. (2019). The relentless march of mass coral bleaching: a global perspective of changing heat stress. *Coral Reefs*, 38(4):547–557.

Sous, D., Tissier, M., Rey, V., Touboul, J., Bouchette, F., Devenon, J.-L., Chevalier, C., and Aucan, J. (2019). Wave transformation over a barrier reef. *Continental Shelf Research*, 184:66 – 80.

Talavera, L., del Río, L., and Benavente, J. (2020). UAS-based high-resolution record of the response of a seminatural sandy spit to a severe storm. *Journal of Coastal Research*, 95(sp1):679.

Westaway, R., Lane, S., and Hicks, D. (2000). The development of an automated correction procedure for digital photogrammetry for the study of wide, shallow, gravel-bed rivers. *Earth Surface Processes and Landforms: The*

Journal of the British Geomorphological Research Group, 25(2):209–226.

Westoby, M., Brasington, J., Glasser, N., Hambrey, M., and Reynolds, J. (2012). 'structure-from-motion' photogrammetry: A low-cost, effective tool for geoscience applications. *Geomorphology*, 179:300 – 314.

Woodget, A. S., Carbonneau, P. E., Visser, F., and Maddock, I. P. (2015). Quantifying submerged fluvial topography using hyperspatial resolution uas imagery and structure from motion photogrammetry. *Earth Surface Processes and Landforms*, 40(1):47–64.

Supplementary Materials for the article:

Structure-from-Motion on shallow reefs and beaches: potential and limitations of consumer-grade drones to reconstruct topography and bathymetry

Authors: C. Gabriel David, Nina Kohl, Elisa Casella, Alessio Rovere, Pablo Ballesteros, Torsten Schlurmann

Photoscan Settings

The study used the SfM and MVS algorithms provided by the software METASHAPE (v1.5.3 Professional, build 8432; agisoft.com) to calculate three dimensional DEM of the increasingly submerged reef flat and adjacent beach area. METASHAPE is a commercial, proprietary software solution by AGISOFT LLC (Agisoft, 2019) and provides several settings, influencing different stages of the SfM-MVS procedure. Table SM-1 contains the settings used in METASHAPE for this study.

Table SM-1. Settings to create the Digital Elevation Model. Settings and values in METASHAPE used throughout this study.

Processing Step	Setting	
Alignment	Accuracy	High
	Reset Current Alignment	✓
	Reference Preselection	X
	Generic Preselction	X
	Key Point Limit	0
	Tie Point Limit	0
	Adaptive Camera Model Fitting	X
Dense Point Cloud	Quality	High
	Depth Filtering	Aggressive
	Reuse Depth Maps	X
	Calculate point Colours	✓
Mesh	Source Data	Dense Cloud
	Surface Type	Hight field
	Depth Maps Quality	Medium
	Face Count	High
	Custom Face Count	200 000
	Interpolation	Disabled
	Point Classes	All
	Calculated Vertex Colours	✓
	Reuse Depth Maps	X
	Use Strict Volumetric Masks	X
DEM	Source Data	Dense Cloud
	Interpolation	Disabled
	Point Classes	All
	Use Custom Region	X
Orthomosaic	Resolution (m)	0
	Surface	Mesh
	Blending Mode	Mosaic
	Hole Filling	✓
	Enable Back-Face Culling	X
	Refine Seamlines	X
	Use Custom Region	X

Dry Ground Control Points

In the manuscript, we consider two survey methods, that have an impact on the alignment procedure in the photogrammetric process. The second approach is done by assuming that only dry areas were accessible and as the water level increases, GCPs becoming wet are neglected in the associated alignment. Table SM-2 contains all GCPs displayed in Fig. 2 and shows whether they have been dry or submerged in the associated flight set and thus if they have been considered in the alignment procedure.

Table SM-2. Dry GCPs. GCPs that are dry (●) or wet (○) in the respective flight sets. In this table, the GCPs are sorted according to their location in Fig. 2, starting from left to right on the beach and advancing towards the seaward GCPs. The GCPs on the beach (17 to 20) are always dry and thus always considered in the alignment, while GCPs 12 and 13 are lying either in a pond or in the deeper section of the channel and are therefore always submerged.

Position within survey-site[1]:	**Beach**				**Water line**			**Center**		**Sea ward**		
GCP number:	**17**	**18**	**19**	**20**	**13**	**3**	**6**	**2**	**4**	**10**	**11**	**12**
Reference Set[2]	●	●	●	●	○	●	●	●	●	●	●	○
Flight set 1	●	●	●	●	○	●	●	○	●	●	○	○
Flight set 2	●	●	●	●	○	○	●	○	○	○	○	○
Flight set 3	●	●	●	●	○	○	●	○	○	○	○	○
Flight set 4	●	●	●	●	○	○	○	○	○	○	○	○

[1] see Fig. 2
[2] see Table 1

Coastline Definition

The manuscript contains an areal overview of deviations between the dry and successively submerged reef – in this study referred to as the areal error made by the SfM algorithm in underwater areas. Fig. 3 displays these over the dry reef's orthophoto and contains the coast- or waterline associated with the reef water level Δh. We defined the waterline by visual observation from the aerial images as displayed in Fig. SM-1

Figure SM-1. Visual coastline extraction. Aerial images of the inundated reef to estimate the coastline for Fig. 3. The images were taken as screenshots from METASHAPE and include the GCP-positions on the images.